remote sensing

IMPACT FACTOR 5.349

CITESCORE 7.9

Article

Contemporaneous Thick- and Thin-Skinned Seismotectonics in the External Zagros: The Case of the 2021 Fin Doublet, Iran

Zeinab Golshadi, Nicola Angelo Famiglietti, Riccardo Caputo, Saeed SoltaniMoghadam, Sadra Karimzadeh, Antonino Memmolo, Luigi Falco and Annamaria Vicari

Special Issue

Technological Advancements in Disaster Damage Assessment Using Earth Observation, Machine Learning, and Numerical Simulation

Edited by

Dr. Bruno Adriano, Dr. Erick Mas, Dr. Luis Angel Moya Huallpa, Dr. Hiroyuki Miura and Prof. Dr. Miguel Estrada

MDPI

https://doi.org/10.3390/rs15122981

remote sensing

MDPI

Article

Contemporaneous Thick- and Thin-Skinned Seismotectonics in the External Zagros: The Case of the 2021 Fin Doublet, Iran

Zeinab Golshadi [1,*], Nicola Angelo Famiglietti [2], Riccardo Caputo [3], Saeed SoltaniMoghadam [4], Sadra Karimzadeh [5,6,7], Antonino Memmolo [2], Luigi Falco [2] and Annamaria Vicari [2]

1 Institute of Geophysics, University of Tehran, Tehran 1417935840, Iran
2 Istituto Nazionale di Geofisica e Vulcanologia, Sezione Irpinia, 83035 Grottaminarda, Italy; nicola.famiglietti@ingv.it (N.A.F.); antonino.memmolo@ingv.it (A.M.); luigi.falco@ingv.it (L.F.); annamaria.vicari@ingv.it (A.V.)
3 Department of Physics & Earth Sciences, Ferrara University, 44121 Ferrara, Italy; rcaputo@unife.it
4 International Institute of Earthquake Engineering and Seismology, Tehran 1953714453, Iran; saeed.soltani@iiees.ac.ir
5 Department of Remote Sensing and GIS, University of Tabriz, Tabriz 5166616471, Iran; sadra.karimzadeh@gmail.com
6 Remote Sensing Laboratory, University of Tabriz, Tabriz 5166616471, Iran
7 Department of Architecture and Building Engineering, Tokyo Institute of Technology, 4259-G3-2 Nagatsuta, Midori-ku, Yokohama 226-8502, Japan
* Correspondence: z.golshadi@alumni.ut.ac.ir; Tel.: +98-9192906527

Abstract: In this work, we propose a geodetic model for the seismic sequence, with doublet earthquakes, that occurred in Bandar Abbas, Iran, in November 2021. A dataset of Sentinel-1 images, processed using the InSAR (Interferometric Synthetic Aperture Radar) technique, was employed to identify the surface deformation caused by the major events of the sequence and to constrain their geometry and kinematics using seismological constraints. A Coulomb stress transfer analysis was also applied to investigate the sequence's structural evolution in space and time. A linear inversion of the InSAR data provided a non-uniform distribution of slip over the fault planes. We also performed an accurate relocation of foreshocks and aftershocks recorded by locally established seismographs, thereby allowing us to determine the compressional tectonic stress regime affecting the crustal volume. Despite the very short time span of the sequence, our results clearly suggest that distinct blind structures that were previously unknown or only suspected were the causative faults. The first Mw 6.0 earthquake occurred on an NNE-dipping, intermediate-angle, reverse-oblique plane, while the Mw 6.4 earthquake occurred on almost horizontal or very low-angle (SSE-dipping) reverse segments with top-to-the-south kinematics. The former, which cut through and displaced the Pan-African pre-Palaeozoic basement, indicates a thick-skinned tectonic style, while the latter rupture(s), which occurred within the Palaeozoic–Cenozoic sedimentary succession and likely exploited the stratigraphic mechanical discontinuities, clearly depicts a thin-skinned style.

Keywords: Bandar Abbas seismic sequence; Fin doublet earthquakes; InSAR measurements; analytical modelling; tectonic deformation; double-difference relocation

Citation: Golshadi, Z.; Famiglietti, N.A.; Caputo, R.; SoltaniMoghadam, S.; Karimzadeh, S.; Memmolo, A.; Falco, L.; Vicari, A. Contemporaneous Thick- and Thin-Skinned Seismotectonics in the External Zagros: The Case of the 2021 Fin Doublet, Iran. *Remote Sens.* **2023**, *15*, 2981. https://doi.org/10.3390/rs15122981

Academic Editors: Hiroyuki Miura, Erick Mas, Bruno Adriano, Luis Angel Moya Huallpa and Miguel Estrada

Received: 8 April 2023
Revised: 29 May 2023
Accepted: 31 May 2023
Published: 7 June 2023

1. Introduction

On 14 November 2021, at 12:07 and 12:08 UTC (17:35 Iran Standard Time for the first quake), Fin doublet earthquakes with M_W 6.0 and 6.4 occurred near the city of Bandar Abbas in the seismically active area of Hormozgan Province, southern Iran (Figure 1 and Table 1). There were about 300 aftershocks following this seismic doublet over the next five months, with 30 aftershocks of a magnitude higher than 4.0 [1,2]. Among them, the largest aftershock of M_w 5.2 occurred on 15 November, potentially causing additional surface displacements. The sequence of earthquakes in Hormozgan killed 1 person, injured 99 people, destroyed 3000 homes, and caused power outages [2].

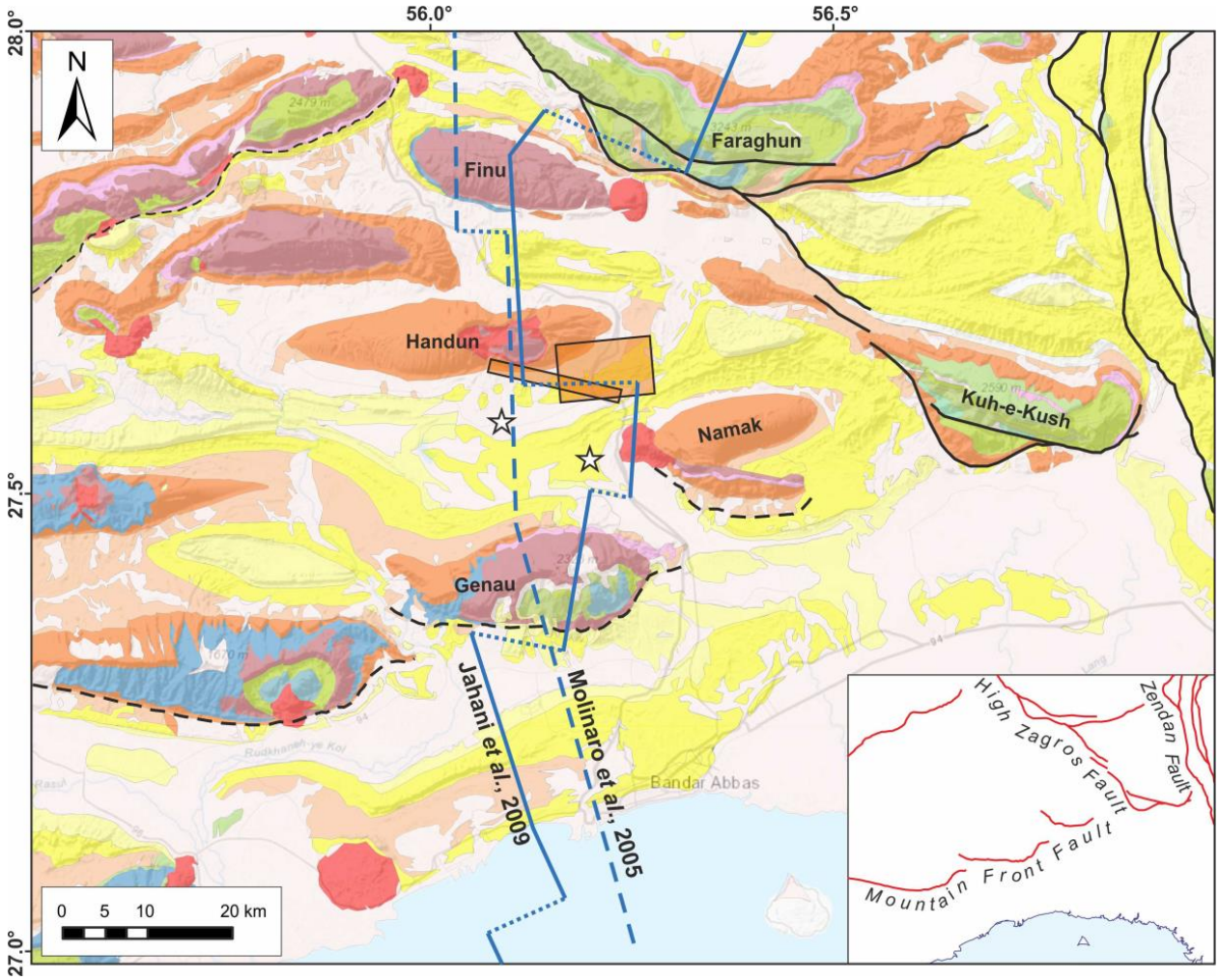

Figure 1. Geological map of the investigated area plotted on a SRTM shaded-relief digital elevation model [3]. The continuous and dashed blue lines (dots for segment connections) represent the traces of the geological profiles by [4,5] discussed in the text. The orange boxes represent the projection on the horizontal plane of the modelled faults. The stars represent the location of doublet earthquakes.

Table 1. Source parameters of the 2021 Fin doublet earthquakes according to several institutions.

Event	Agency	Dataset	Magnitude	Plane n.	Strike (°)	Dip (°)	Rake (°)	Depth (km)	Lat. (°)	Lon. (°)
1	USGS	Teleseismic	6.0 (M)	1 2	270 91	63 27	90 91	9	27.716	56.074
	GCMT	Teleseismic	6.1 (M_w)	1 2	262 105	56 36	77 108	17.2	27.570	55.980
	IRSC	Regional seismic data	6.2 (M_N)	- -	- -	- -	- -	19.5	27.568	56.084
	IIEES	Regional seismic data	6.3 (M_L)	-	-	-	-	14	27.668	56.075
	EMSC	Regional seismic data	6.0 (M_W)	-	-	-	-	10	27.71	56.12
	GFZ	Teleseismic	6.0 (M_W)	-	-	-	-	10	27.65	55.99
2	USGS	Teleseismic	6.4 (M)	1 2	289 41	85 12	101 22	10	27.727	56.072
	GCMT	Teleseismic	6.1 (M_w)	1 2	276 75	65 27	99 72	13.8	27.54	56.03
	IRSC	Regional seismic data	6.3 (M_N)	-	-	-	-	10.0	27.536	56.174
	IIEES	Regional seismic data	6.4 (M_L)	-	-	-	-	15	27.565	56.367
	EMSC	Regional seismic data	6.3 (M_W)	-	-	-	-	10	27.73	56.15

These earthquakes occurred within the tectonically active area situated at the eastern tip of the Zagros Fold-and-Thrust Belt (ZFTB) (southern Hormozgan Province) [6]. The ZFTB belongs to the broader Alpine-Himalayan orogenic belt and is located in the northern sector of the Arabian plate and the Persian Gulf. As a result of the ongoing collision between the Arabia and Central Iran plates, the Zagros Mountains were formed [7]. Salt diapirs from the Late Precambrian Hormuz salt are abundant in the eastern Zagros, as are collision-related detachment folds with irregular shapes along-strike. The salt diapirs in this area (plugs and domes) are irregularly distributed from the suture zone in the north to the Persian Gulf and in the south [8] (Figure 1), and they play a crucial role in the tectonic evolution of the region. Short and compact fold structures form on top of a major detachment [9] and accommodate most of the shortenings in the deformed parts of the area [4,10,11]. The fold location, the orientation of the hinge axis and their shape and size are strongly influenced by preexisting salt features and local pre-buckling thickening. In addition, salt structures generate small basin geometries, which consequently govern the sedimentary distribution and facies [5,12].

Changes in the fold axis trend in the Genau, which is a buried salt diapir, as well as salt plugs (such as the Handun and Finu) are evident in this area. There was a probable salt diapir uplift process in this area since the Palaeozoic era [13]. The salt dome of Handun, which emerged in the core of the Handun anticline and is responsible for its peanut shape, was supposed to be inactive. [12]. Shortening across the area occurs at a rate of ~20 mm/a [14], which is partly accommodated along the subduction interface separating the underthrusting oceanic crust from the overlying south-eastern Zagros accretionary wedge [15].

Early NW–SE trends, such as those controlling the deposition of the Cambrian Hormuz salt unit, are thought to be inherited from late Precambrian deformation [15]. According to [16], the overall strain field across the Zagros is directed N–S to N010° on average and is slightly oblique at ~20–30° relative to the long-term SW–NE shortening direction across the orogen. The maximum compressive strain orientation in the SE Zagros has been found to be oriented 14–18°, and the convergence rates characterising the area increase from NW to SE [4,17,18]. The anticlinal structures located along the SE margin of the orogen are associated with major topographic features and present the highest elevations in the SE Zagros, exposing rocks as old as the Ordovician and Cambrian periods with respect to their cores [13,19]. As a result of the Late Ordovician transgression, shales, siltstones, sandstones, and fossiliferous limestones were deposited [13].

The Eo-Cambrian-to-Quaternary sedimentary cover of the Arabian plate shows a maximum thickness of 10–12 km in correspondence with the eastern sector of the ZFTB [5,20]. This sequence consists of mainly Palaeozoic and Mesozoic successions overlain by Cenozoic siliciclastic and carbonate rocks resting on top of a highly metamorphosed Neoproterozoic Pan-African basement that has been impacted by major transcurrent shear zones [20–22].

Between the sedimentary units and the basement rocks, there exists a high competence-mechanical contrast, where a major detachment level has developed. From this weakness zone, diffuse folding develops [4], while the underlying basement is characterised by low-angle shear zones accommodating the shortening [23]. It is worthwhile to note that the sector of the chain where the Fin doublet occurred, which is delimited to the north by the High Zagros Fault (HZF) and to the south by the Mountain Frontal Fault (MFF; Figure 1), was also referred to in the past as the "Zagros Simply Folded Belt" [23–25].

The emergent salt domes in the east Zagros area reveal that halokinesis (internal trigger) prevails over tectonic processes (external trigger), and the rifting event that occurred during the Palaeozoic was the main factor giving rise to the Hormuz diapirism. Additionally, in subsequent deformational events, these emergent diapirs played a crucial role in the location, geometry and kinematic evolution of faults and folds [26].

In this paper, to identify the major causative faults of the seismic sequence and better understand the seismotectonics of the study area, we present a multi-disciplinary study combining seismological and geodetic data with the geological and tectonic information

available for the region. Using the InSAR (Interferometry from Synthetic Aperture Radar) two-pass technique, we reconstructed some major active faults affecting the area [27], with the aim of contributing to a better understanding of the seismotectonic evolution of the broader region and particularly its seismotectonic characteristics. For this purpose, we proposed a realistic parametric model of the causative faults associated with the evolution of the area based on inversion techniques of ground deformation detected by the InSAR, the compilation of tectonic data, the analysis of foreshock and aftershock sequences and the calculation of the coseismic stress drop. The flowchart of our procedure is presented in Figure 2.

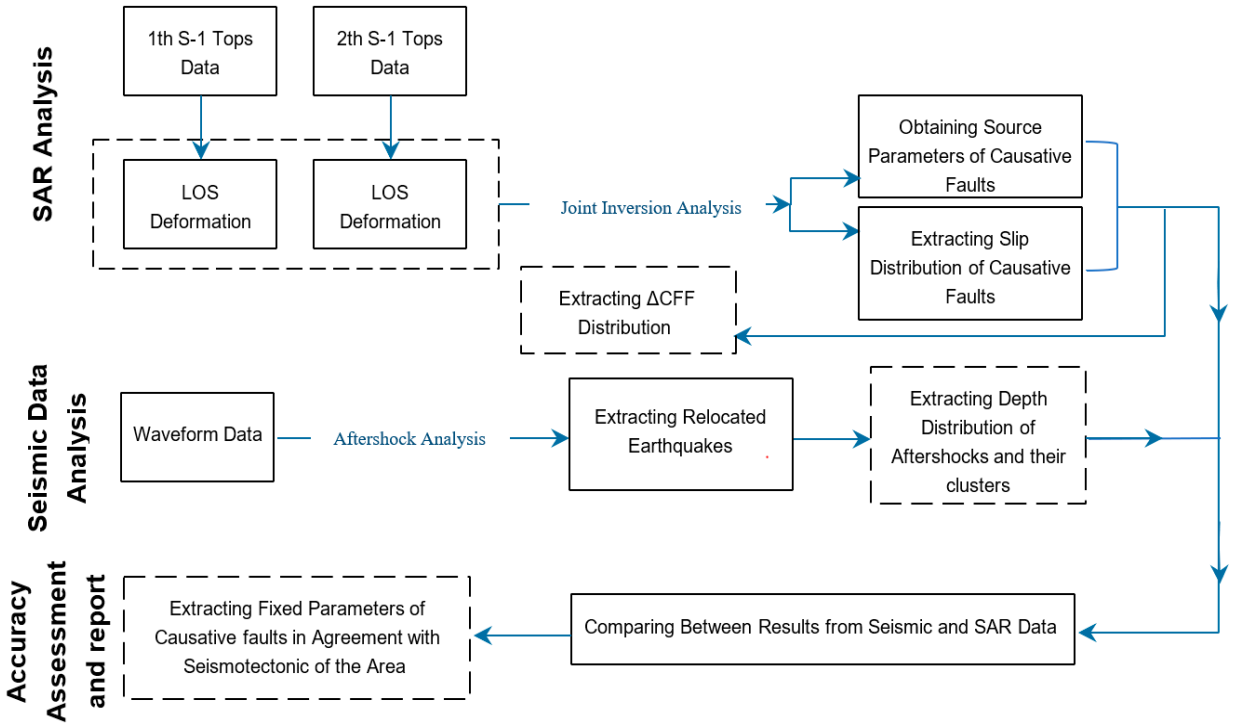

Figure 2. Flowchart of our procedure in this study.

2. Materials and Methods

2.1. InSAR Deformation and Fault Model

SAR imaging from space, based on the DInSAR (Differential Interferometric Synthetic Aperture Radar) technique, is routinely used to monitor coseismic surface displacements. The use of two satellite images taken before and after an earthquake allows the DInSAR to reconstruct the coseismic motion [28]. This research is based on Sentinel-1 satellite imagery, obtained from the ESA (European Space Agency) constellation, in IW (Interferometric Wide) mode and V–V polarisation with a wide 250 km swath coverage, and enables near-real-time response to seismic events [29–31]. Coseismic displacement fields were retrieved using two pairs of images along the ascending and descending orbits, at a temporal interval of 12 days (Table 2). Due to the minimal time gap between the two events, both pairs obviously include the mainshocks. Additionally, several aftershocks occurred during the time window, but their contribution in terms of surface deformations was likely negligible.

Table 2. Sentinel-1 pairs used to detect the permanent deformations of the Fin doublet mainshocks and major aftershock.

Interferogram Number	Master's Date	Slave's Date	Pass Direction	Orbit Number
1	13 November 2021	25 November 2021	Ascending	57
2	9 November 2021	21 November 2021	Descending	166

A final ground resolution of about 30 m was achieved by co-registering and multi-looking 4 and 1 in the range and azimuth directions, respectively., thereby increasing the signal-to-noise ratio. Orbital corrections were then applied using ESA PO (Precise Orbits), and the SRTM-1 digital elevation model was used to remove the topographic phase contribution.

We significantly improved the quality of the interferometric fringes by applying an adaptive filtering algorithm to the raw interferograms [32]. As compared to using fixed filter parameters [33–35], adaptive filtering algorithms allow one to adjust the filter parameters according to the current input, which can improve filtering performance. In addition to self-tuning, robustness, real-time operation and reduced complexity, the adaptive filtering algorithm has some disadvantages, e.g., computational complexity, requiring a significant amount of time and data to converge and sensitivity to initialization. The unwrapping interferogram was obtained using a MCF (Minimum Cost Flow) algorithm [36] and then geocoded using the same 30 m resolution SRTM-1 DEM.

Any interferometry measures motion along a satellite's line of sight (LoS), i.e., the oblique direction between the satellite and the Earth's surface. Positive values along the LoS correspond to a movement of the ground towards the satellite, while negative values indicate a movement away from the satellite (Figure 3).

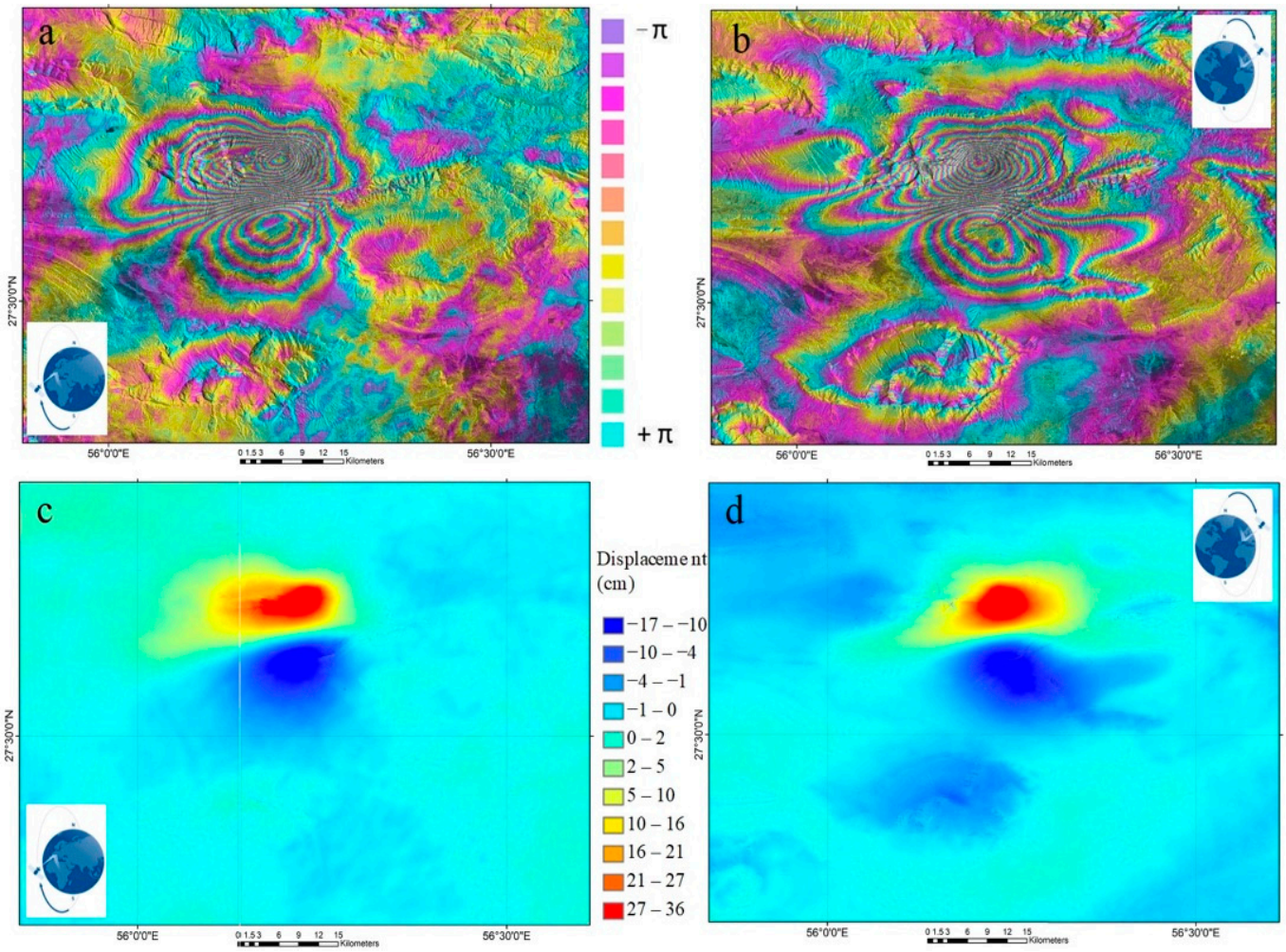

Figure 3. Interferometric fringes (**a**,**b**) and displacement maps (**c**,**d**) for ascending (**left**) and descending (**right**) orbits for the 2021 Fin doublet earthquakes. When a displacement is positive, it indicates that the earth is moving towards the satellite, while when it is negative, it indicates that the earth is moving away from it.

We modelled a subset of points sampled from ascending and descending raster maps, which had been acquired by posting images every 500 m in the close range and 2000 m in the far range, to retrieve the parameters of a finite dislocation source. The LoS coseismic points from two orbits were then jointly modelled using a validated dual-step approach: first, the geometry and position of the fault were determined by a nonlinear inversion. Subsequently, a linear inversion was carried out to determine the slip distribution on the inverted fault planes. There was a different contribution of post-seismic motion to each coseismic displacement map based on the temporal coverage. For both cases, the geophysical model for predicting surface displacement was the elastic finite dislocation source in a homogeneous half-space [37]. More details about both steps implemented in this study are described in [38–40].

Non-linear inversion was carried out using the Levenberg–Marquardt optimization algorithm [41]. A minimization algorithm that restarts multiple times can ensure that the global minimum is captured. It is an efficient method for dealing with nonlinear problems with many variables. In comparison to other algorithms [42–44], this technology has several advantages: it is more robust than the Gauss–Newton method; it converges faster than either gradient descent or GN on their own; it can handle models with multiple free parameters that are not known precisely. Even if one's initial guess is incorrect, the LM can still find an optimal solution; however, if there are more than 10 parameters in a model, the convergence time can be very slow. The linear inversion procedure preserved the fixed geometric settings derived from the non-linear inversion and spread the fault until the slip vanished to zero [38]. Trial-and-error was used for the damping of the system, with the empirical parameters balancing the slip distribution roughness and data fit [45,46]. Our non-negative constraint prevented the slip direction from changing along the fault.

Using the Coulomb stress field, it was also possible to determine whether the second shock and most aftershocks occurred in areas of increased stress. The complexities of fault networks and their intersections might contribute to through-going ruptures and large multi-segment earthquakes [47]. We therefore postulated that a triggering effect was induced by the first fault and estimated how the stress changed on other nearby faults. The static analysis of the Coulomb failure function (ΔCFF) was constrained with the plane geometries and rake directions from the non-linear inversions [48].

2.2. Analysis of Aftershocks

The aftershock sequence of the Fin doublet earthquakes was not collected by a very dense local seismological network. We prepared data by combining recorded pick phases from 23 seismic stations (Figure 4) belonging to the IRSC catalogue (www.irsc.ir (accessed on 7 April 2023)) [1] and the IIEES catalogue (www.iiees.ac.ir (accessed on 7 April 2023)) [2] and from one station belonging to the national seismic network of the UAE. The nearest and farthest stations are BNDS (IIEES) and KSHD (IRSC), with mean distances of 15 km and 350 km, respectively, to the cluster centroid. The initial dataset consists of 383 earthquakes (Ml > 2.5) that started one month before the mainshocks and lasted for six months (1 August 2021 to 30 May 2022).

The total numbers of P and S phases are 2818 and 268, respectively, which were identified manually by each network's operator. To relocate all earthquakes, we used an updated version of the 1D velocity model (Table 3) based on [49,50], located in the south west of the study area.

To reduce location uncertainty for these closely spaced events, we employed the double-difference earthquake location method, HypoDD [51]. This method is particularly useful to map the aligned distributions of earthquakes that may highlight the fault geometry. We used a selected subset of 364 events according to the quality criteria described in the HypoDD document [52] for defining the strong linkage between closely spaced events. By considering easy to harsh conditions using different parameters for both selecting catalogue data and running HypoDD, we obtained a maximum resolution image of seismicity and eliminated any relative scatter in location caused by local heterogeneities in the assumed

1D velocity structure. We applied the nearest-neighbour approach to link the events using a maximum search radius of 10 km (MAXNGH) and a minimum number of 8 links (MINLNKS), each with a minimum number of 6 observations (MINOBS), and selected a maximum separation of 10 km (MAXSEP). Event linkage strongly controls how well a dataset will be relocated in HypoDD. Ultimately, the HypoDD program reduced the dataset of 364 events to 280 events during the relocation process, all in one cluster.

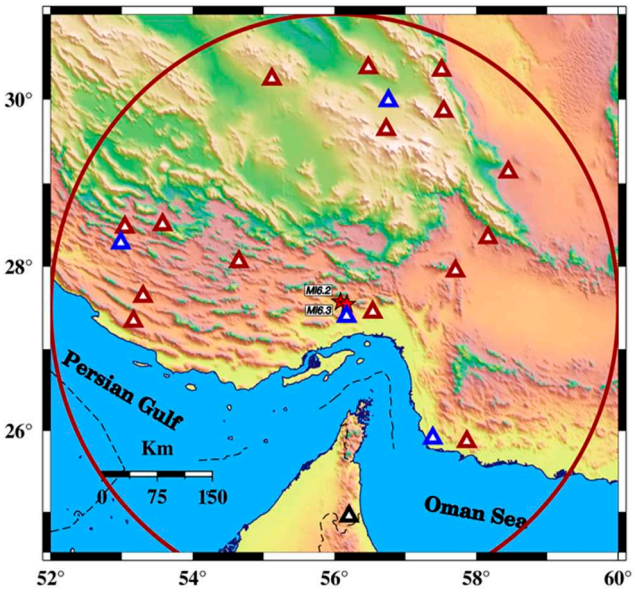

Figure 4. Fin doublets recorded by regional networks. The red, blue, and black triangles denote seismic stations belonging to the IRSC, IIEES, and UAE, respectively. The red circle shows the area within a 350 km radius from the mainshocks. The red stars represent the location of doublet earthquakes.

Table 3. Updated velocity model used in this study.

Layer	Vp (km/s)	Z (km)
1	4.20	0.0
2	5.40	2.0
3	5.70	4.0
4	5.90	10.0
5	6.10	14.0
6	6.50	19.0
7	8.20	46.0

3. Results

There was a significant increase in the seismicity rate in the Fin area of Hormozgan Province as a result of two strong mainshocks on 14 November 2021. With the use of the SAR acquisition, two events were included in the analysed time window (Table 1). Due to the fact that a differential interferogram's coherence factor largely depends on the reference image's temporal baseline and spatial decorrelation [53], a short time interval was used in this study to produce interferograms with good coherence gaps (>0.6).

Given that the seismicity was relatively tightly spaced, we were able to characterise the aftershock sequence, among different runs of HypoDD, as a single cluster of 280 earthquakes (Figure 5), which were mostly located at the western edge of the MFF. Based on the event location accuracy as defined in Table 4, all events were subdivided into three subclasses. As a result, 20, 110 and 225 events occurred in subclasses A, B and C, respectively. About 50% of the aftershocks had a depth uncertainty of less than 3 km, and about 78% had a depth uncertainty of less than 4 km (Figure 6).

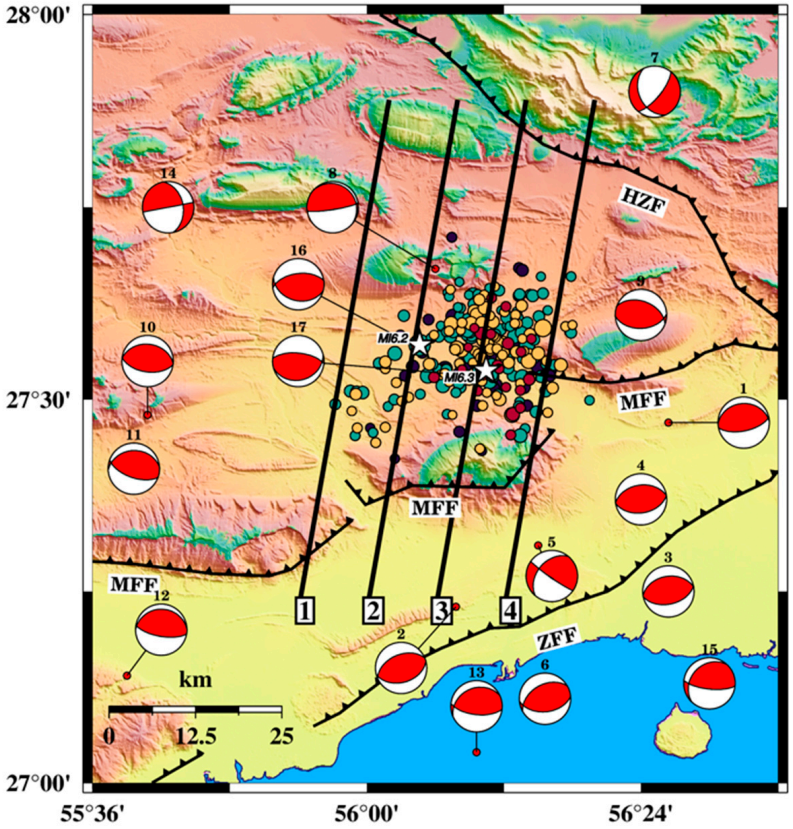

Figure 5. Fin doublet earthquakes (white stars) and aftershocks (coloured based on location accuracy in the three subclasses A, B and C (Class A: red; class B: orange and class C: green)). All focal mechanisms (in red) were obtained from the GCMT. Four depth cross-sections are depicted in black lines. HFZ: High Zagros Fault; MFF: Mountain Front Fault; ZFF: Zagros Frontal Fault.

Table 4. Statistical parameters for defining subclasses A, and B and C.

Class	Horizontal Error (km)	Depth Error (km)	RMS (s)	Azimuthal Gap (°)	Number of Events
A	2.0	4.0	0.3	180	20
B	3.0	6.0	0.4	200	110
C	5.0	8.0	0.5	200	225

Body-wave modelling determined the centroid depth of moderate-sized earthquakes throughout the Zagros [49,54–56], i.e., between about 8 and 20 km. Looking at the depth distribution of the relocated events (Figure 6), it is possible to observe that ca. 90% of the recorded seismicity occurs within the first 20 km, showing a higher density between 7 and 20 km and a peak at 12–15 km. Taking into account the depth errors (Figure 7b), the depth distribution and the cluster (Figure 8) seem to confirm that most seismogenic deformations occur in the deeper layers of the sedimentary cover and mainly within the underlying basement rocks, where rheological behaviour is fundamentally brittle and frictional processes prevail [57]. This confirms that crustal deformation is still active in this sector of the Zagros and especially documents the persistent seismogenic behaviour of the tectonic structures pervading the area at this depth.

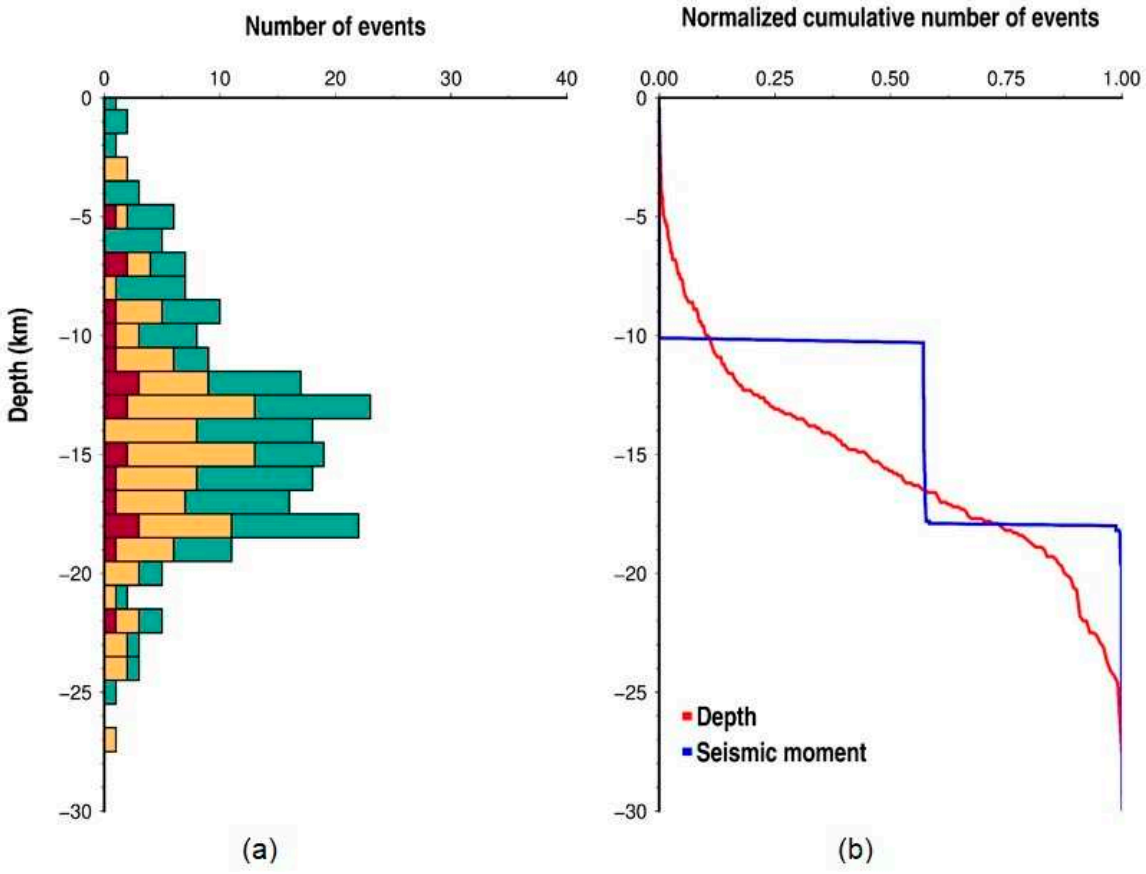

Figure 6. Depth distribution of the relocated aftershocks represented as (**a**) a histogram, based on their quality ranking (red: A; orange: B and green: C), and (**b**) normalised cumulative curves both as number (red) and energy (blue).

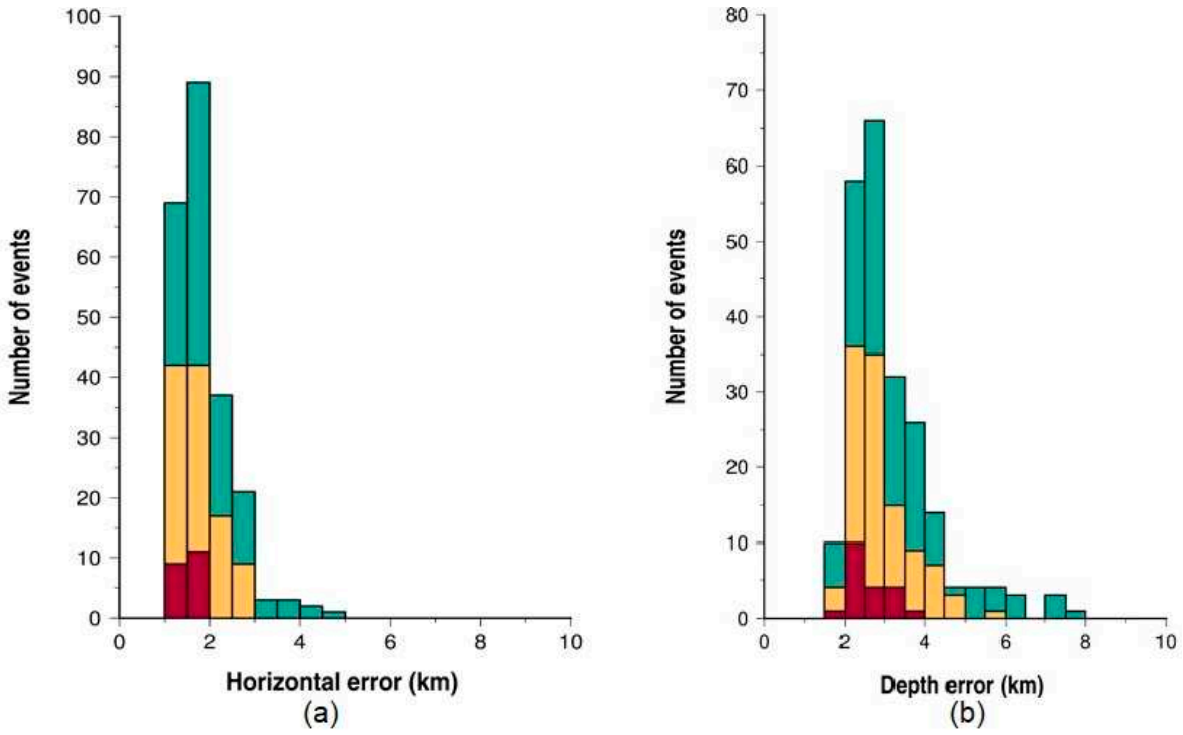

Figure 7. Horizontal (**a**) and depth (**b**) uncertainty distributions based on the three subclasses reported in Table 4. Class A: red; class B: orange and class C: green.

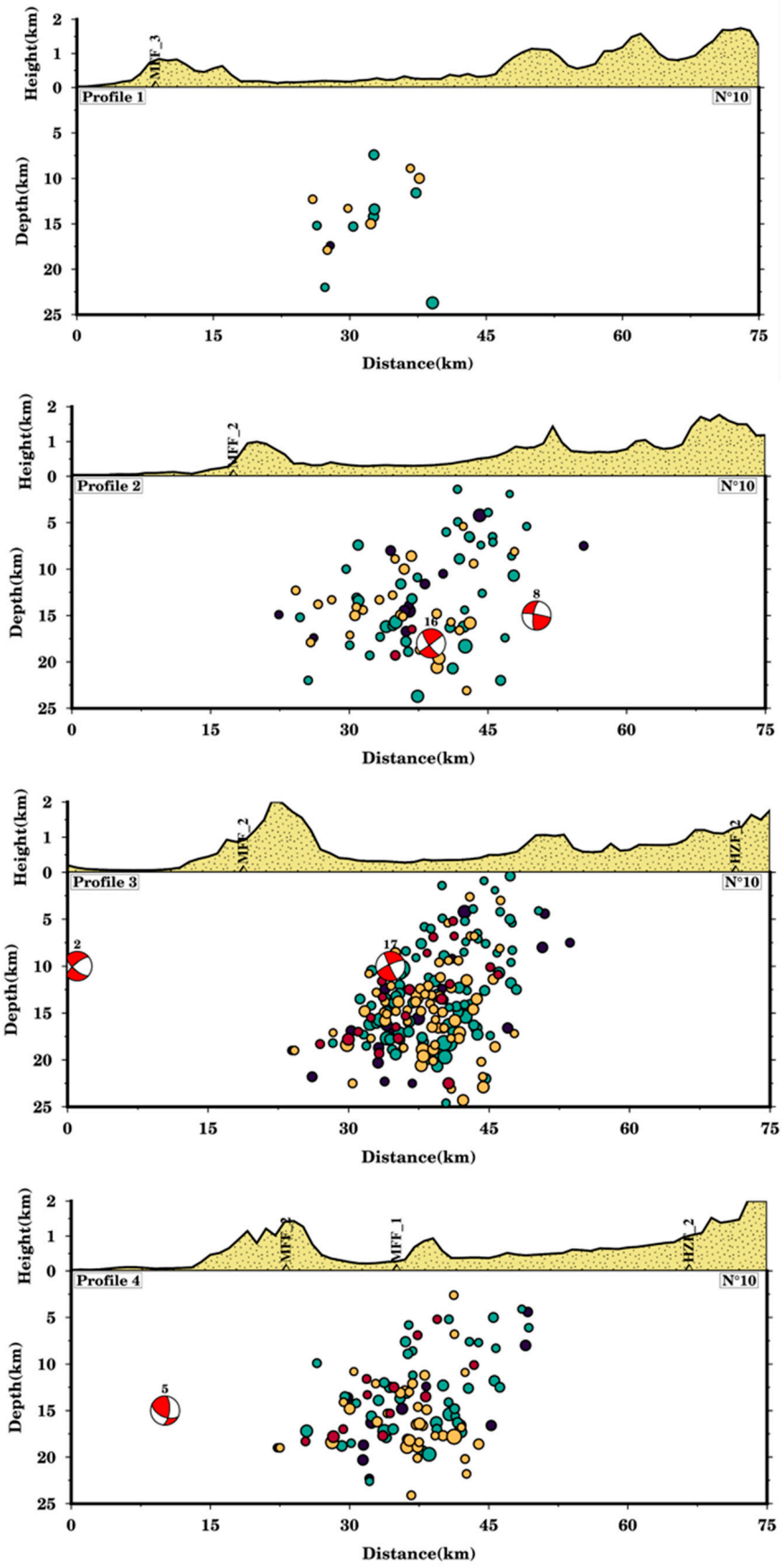

Figure 8. Depth cross-sections and focal mechanisms showing a clear view of a new reverse fault with a southward dip. The events are coloured based on the three subclasses.

With precise earthquake locations associated with focal mechanisms listed in Table 5 (Figure 5), it is possible to determine the geometry and motion of active faults and their location with respect to thick sedimentary layers [6,58,59]. Most of the focal mechanisms in the Central Zagros are based on the CMT catalogue or computed from body-wave modelling [54–56,58]. The majority of moderate-to-big earthquakes occurred on reverse faulting on the planes oriented NW–SE (Figure 5, Table 4). In Figure 5, the reverse mechanisms #8, 9, 16 and 17 trend northwest–southeast and parallel to the fold axes. Figure 5 shows a consistency between the trend of the aftershocks and the strike of reverse-faulting mechanisms and suggests that they are clearly related to the shortening on the planes striking NW–SE.

Table 5. Focal mechanism solution provided by the GCMT. All values have been checked from the GCMT website.

No.	Date–Time	Lon (°)	Lat (°)	Depth (km)	Mw	Strike (°)	Dip (°)	Rake (°)
1	21 March 1977 21:19:04	56.44	27.47	18.8	6.7	267	27	98
2	22 March 1977 11:57:35	56.13	27.23	10.0	5.9	75	43	96
3	23 March 1977 23:51:19	56.44	27.25	10.0	5.5	261	41	92
4	1 April 1977 13:36:30	56.40	27.37	10.0	5.9	262	44	90
5	16 April 1981 10:27:18	56.25	27.31	15.0	5.1	221	42	8
6	12 July 1983 11:34:22	56.26	27.11	46.0	6.0	241	45	73
7	18 December 1987 16:24:05	56.42	27.90	15.0	5.8	155	39	−149
8	9 June 1988 00:09:49	56.10	27.67	15.0	5.2	310	11	139
9	5 March 2006 09:40:08	56.40	27.61	33.0	5.4	290	45	106
10	25 March 2006 09:55:16	55.68	27.48	12.0	5.5	276	35	89
11	25 March 2006 10:00:38	55.66	27.41	12.0	5.2	267	30	70
12	24 July 2007 10:08:01	55.65	27.14	20.0	5.0	270	21	81
13	3 November 2009 23:26:53	56.16	27.04	13.2	5.0	246	30	63
14	10 November 2014 13:52:39	55.71	27.75	15.0	5.2	349	41	180
15	30 December 2019 13:49:46	56.50	27.13	18.0	5.2	223	28	41
16	14 November 2021 12:07:04	55.98	27.57	17.2	6.1	105	36	108
17	14 November 2021 12:08:39	56.03	27.54	13.8	6.1	75	27	72

We jointly modelled the dataset of the points sampled from the InSAR data, assuming that the dislocation occurred over a single surface simplified as planar geometry, for which all parameters were left free in the non-linear inversion. The analysis of the InSAR images indicated that the deformation area nearly coincided with the northern aftershock cluster. From the inversion of the InSAR data, a geodetic solution of the seismic sources was produced providing the following values: 284°/53°/92° (strike, dip angle, rake) and 85°/6°/81°, respectively, for the two doublet events. Accordingly, the first modelled plane corresponded to the NNE dipping dip-slip fault with purely reverse kinematics. The second quake corresponded to the SSE low-angle reverse fault. The geodetic seismic moments calculated based on Okada's formalism were 2.41×10^{18} N·m and 3.5×10^{18} N·m, corresponding to Mw 6.0 and Mw 6.4, respectively.The results of the non-linear modelling suggest uniform slip sources with length and width of 15.5×3 km^2 and 11×7 km^2, respectively. Based on the comparison between observed and predicted surface displacements using the Okada modelling, as well as the residuals, the solutions obtained were basically reliable and well-fitted; Figure 9 shows the signals derived from linear least-squares inversions of the observed, modelled and residual data.

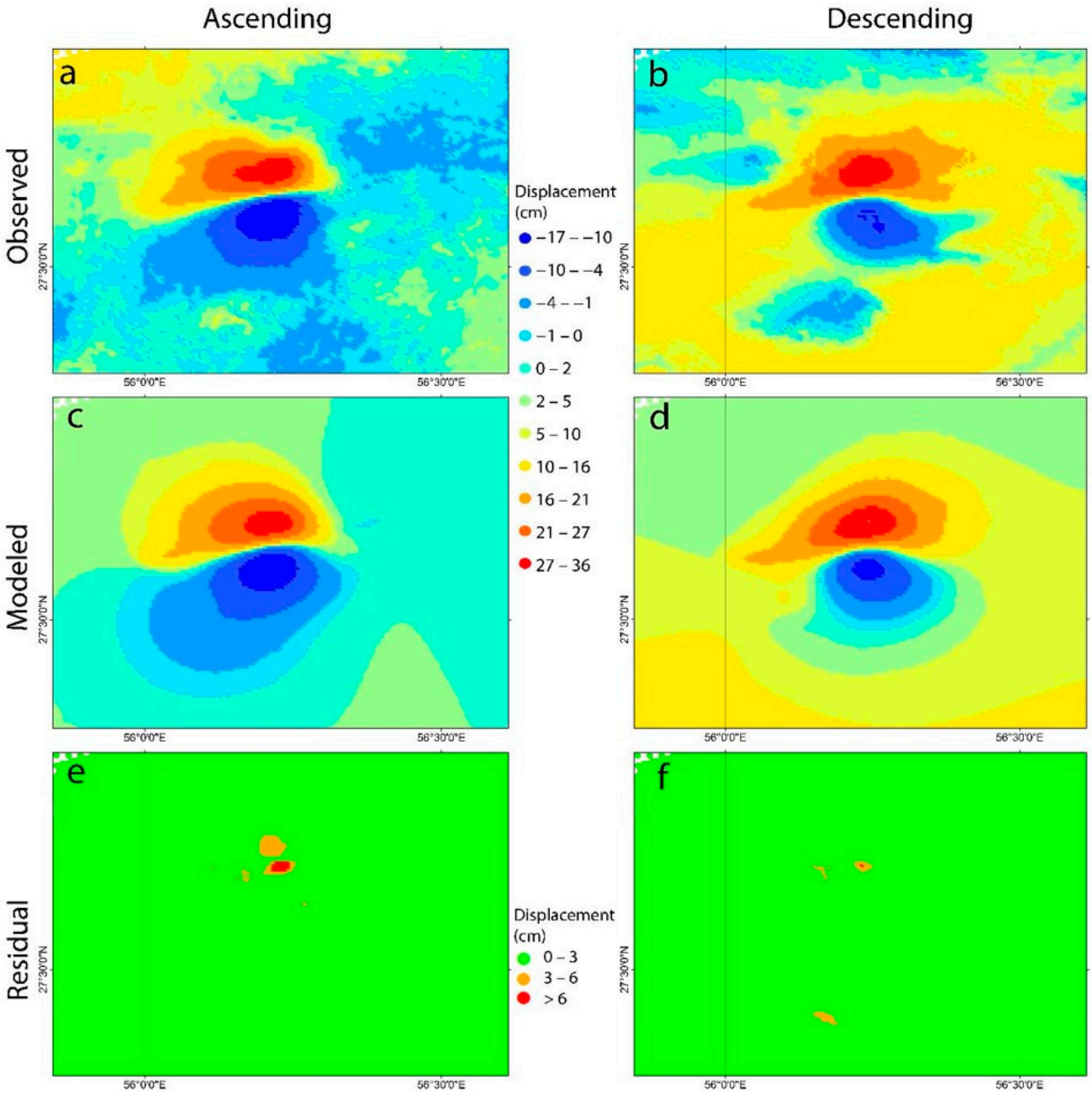

Figure 9. Observed (**a**,**b**), modelled (**c**,**d**) and residual (**e**,**f**) maps for displacements obtained from the ascending and descending orbits for the Mw 6.0 and 6.4 doublet mainshocks.

This preliminary model was then used for the linear inversion, where the planes were subsampled into subareas of 1 × 1 km to better and more realistically reconstruct the slip distribution on the rupture surfaces. The results for the first quake showed a single slip peak distribution that reached the highest value (~90 cm) at a depth of ~11 km, with most of the dislocation included between about 7 and 14 km depth (Figure 10). For the second event of the seismic doublet, most of the slip occurred at depths from 1 to 7 km, while a maximum value of ~252 cm was obtained at a depth of about 5 km.

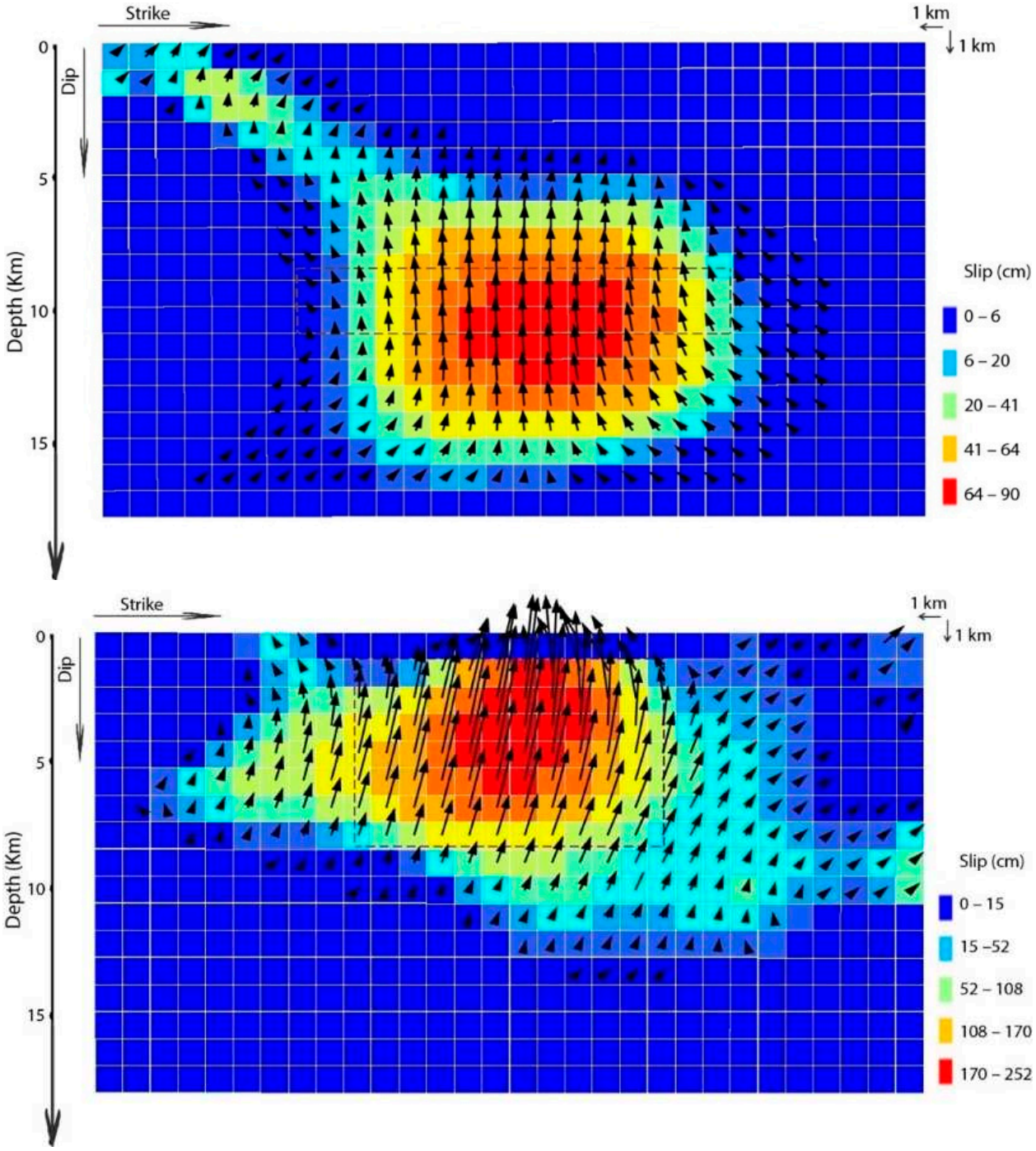

Figure 10. Slip distribution of the Mw 6.0 (**top**) and Mw 6.4 (**bottom**) mainshocks of the Fin doublet earthquake (the view is from the south side). The dashed lines show the result of non-linear inversion, and depth is along the dip of the faults.

Using standard elasticity theory with known seismogenic fault parameters, the change in the stress field can be predicted, and its impact on nearby faults can be quantitatively assessed by evaluating a Coulomb Failure Function (CFF). [60]. The induced stress of the first earthquake (triggering event) on the fault plane, which was reactivated by the second event of the doublet sequence (receiving fault), is shown in Figure 11. The positive ΔCFF values indicate that the main event induced subsequent faults toward failure, while the negative ΔCFF values indicate fault relaxation and failure-time delay.

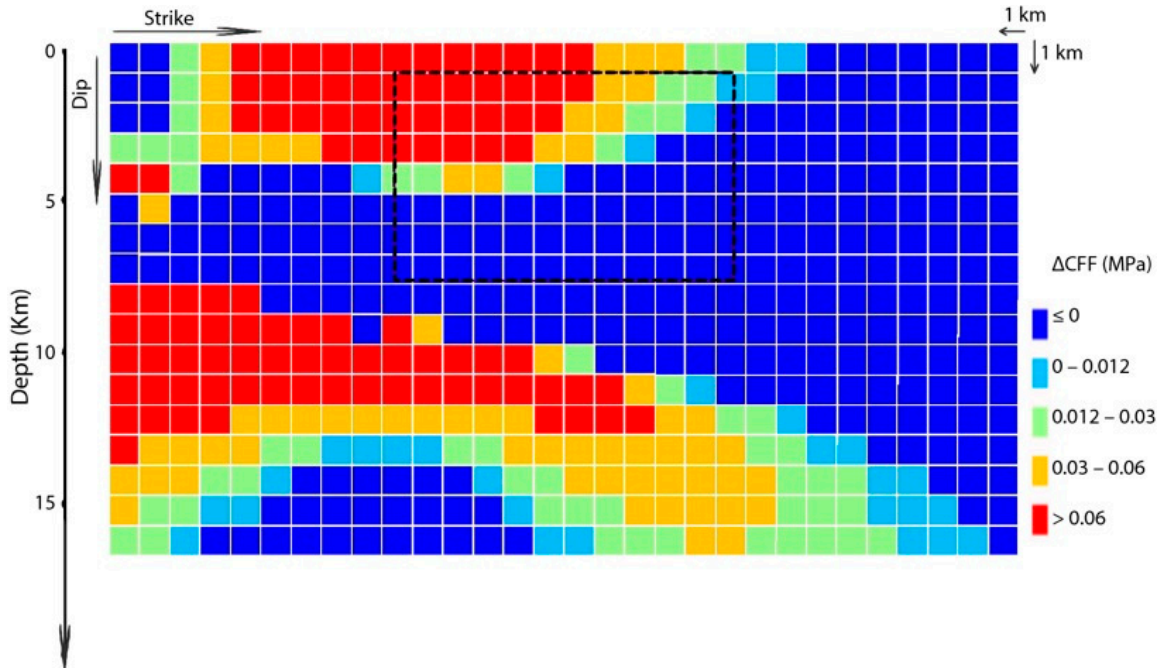

Figure 11. Distribution of the ΔCFF on the modelled fault plane (receiving fault), which was reactivated by the second mainshock of the doublet sequence as a consequence of the first earthquake (triggering fault). The dashed line shows the location of the maximum slip of the receiving fault (the result of non-linear inversion).

4. Discussion

In order to identify the major causative faults of the seismic sequence and shed light on the seismotectonics of the study area, we systematically revised the geological and tectonic reconstructions available for the broader investigated region with special emphasis on the epicentral area. Indeed, several authors (e.g., [4,5,23,61–63]) have proposed geological cross-sections across the central and southeastern Zagros Fold-and-Thrust Belt and particularly across the Zagros Simply Folded Belt, which was affected by the Fin seismic sequence (Figure 1). All of these sections are commonly based on the interpretation of seismic reflection profiles, boreholes for hydrocarbon exploration, geological field observations and seismic data. Most of the published profiles are declared to be balanced.

As a matter of fact, the depths and consequently the geometry of stratigraphic units, as well as of the tectonic structures, are better constrained in the shallower sectors of the profiles, while uncertainties generally increase downwards (e.g., [4]). For example, in correspondence with the epicentral area, the bottom of the post-Hormuz sedimentary succession (from Palaeozoic to present) has been proposed to be at depths varying between 7.5 and 14 km (Figure 12). Similarly, and even worse due to the velocity inversion within the Late pre-Cambrian evaporites, the thickness of the Hormuz Formation and especially the depth of the Pan-African crystalline basement could vary among different authors. For example, the top of the mid-crustal crystalline rocks has been proposed in different interpretations to be at depths varying between 8 and 15 km (Figure 12).

Some differences in tectonic style could also be due to the diverse sensitivity of researchers and the role they have attributed to folding, faulting and/or diapiric phenomena. Nevertheless, all profiles basically agree on two main aspects. Firstly, they implicitly or explicitly suggest the occurrence of a major subhorizontal shear zone (sometimes referred to as basal detachment) in correspondence with the highly mobilised Hormuz evaporitic succession. Secondly, they draw large-scale folds that typically have half wavelengths from 5 to 15 km. It is also worth mentioning that in all profiles, deep-seated intermediate- to high-angle faults are proposed to have affected the Proterozoic mid-crust underlying the Hormuz Formation.

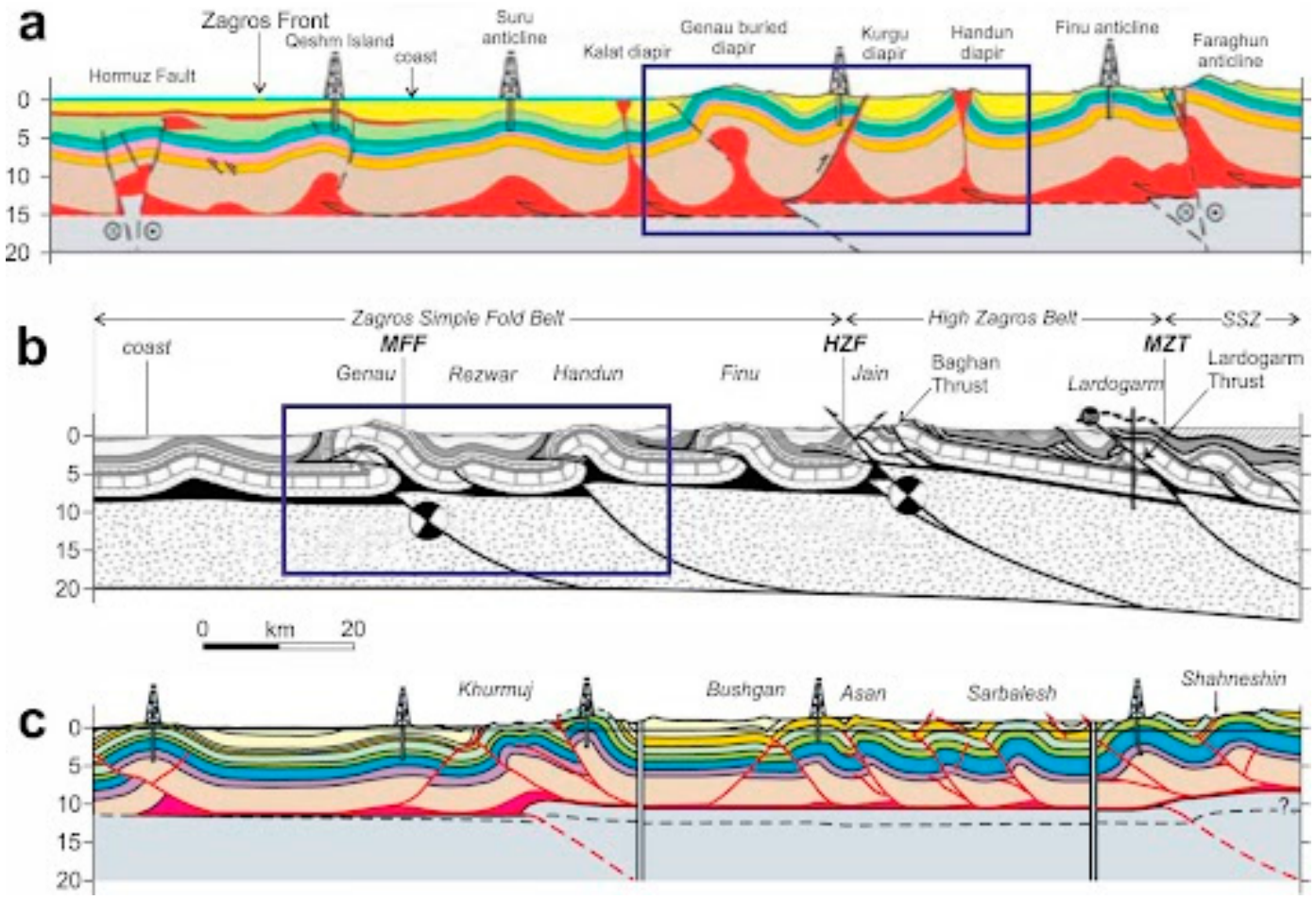

Figure 12. Three examples (**a**–**c**) of geological profiles reconstructed across the central southeastern sector of the Zagros Simply Fold Belt (modified from [4,5,61]). The blue boxes in (**a**,**b**) indicate the seismogenic volume shown in more detail in Figure 13.

Two of the above-mentioned profiles from [4,5] are of particular interest for the goals of the present research as they have been reconstructed exactly across the epicentral area of the Fin seismic sequence (Figure 13). Their traces are presented in Figure 1.

For the purpose of this paper, we redrew these two profiles focusing on the sector between the Genau and Handun anticlines. It should be noted that both profiles were segmented, composited and reconstructed by the authors on the basis of distinct non-parallel seismic profiles; as a consequence, although the traces are roughly parallel to each other, they run a distance between 1 and 13 km, and this has an obvious impact on the originally proposed interpretations. Taking into account the above-mentioned uncertainties, we slightly modified the deeper portions of the drawings in an attempt to provide a uniform interpretation, especially regarding the depth of the mid-crustal basement top and the thickness of the post-Hormuz Palaeozoic stratigraphic units. On the other hand, the vicinity of the two profiles and, in some parts, their superposition could not justify the major differences in the geological and tectonic reconstructions. Thus, these differences had to be minimised.

As described and discussed in the previous sections of this paper, the rupture surfaces associated with the Fin mainshocks were geodetically and seismologically modelled. Based on the reconstructed 3D geometries, we plotted the intersections of the modelled seismogenic sources on the two geological profiles as shown with thick red curves in Figure 13.

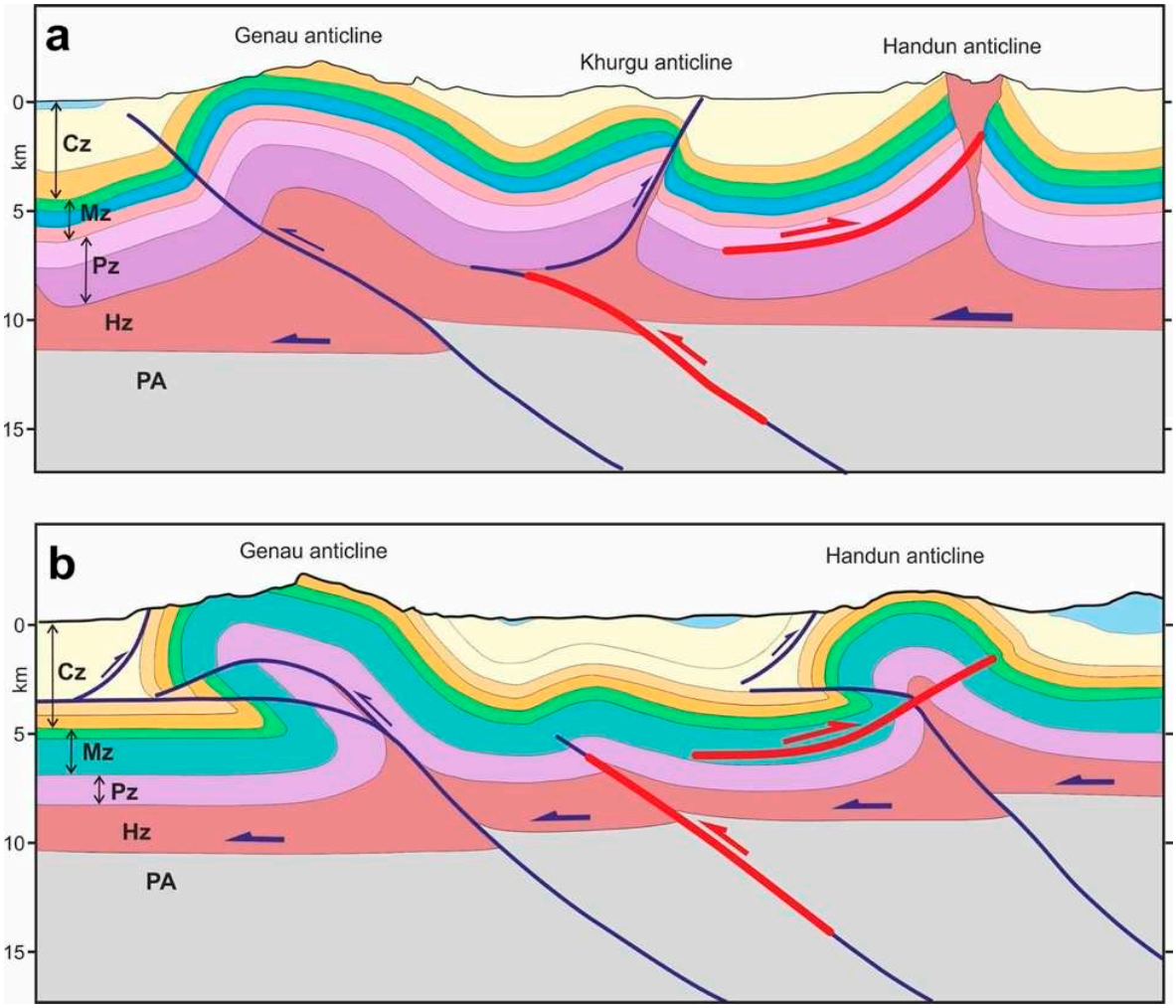

Figure 13. Geological profiles across the epicentral area, modified from [5] (**a**) and [4] (**b**). The red curves represent the causative faults of the Fin seismic sequence mainshocks based on the modelling proposed in the present paper. The blue curves represent probable faults extracted from other studies. PA: Pan-African mid-crustal basement; Hz: pre-Cambrian Hormuz Formation; Pz: late pre-Cambrian and Palaeozoic; Mz: Mesozoic units; Cz: Cenozoic units.

The results of this exercise are quite interesting because they indicate that the first main shock of the Fin doublet clearly reactivated a 'basement' fault characterised by an intermediate-angle setting and dip-slip reverse kinematics. The presence and recent tectonic activity of similar deep-seated faults, which likely exploit the inherited mechanical discontinuities within the Pan-African crust, are well documented within the Zagros, mainly based on seismological and morphological evidence [4,6,11,59,64–66].

Regarding the second mainshock of the Fin doublet, it certainly occurred within the Palaeozoic–Present sedimentary succession overlying the basal detachment developed in the Hormuz Formation. Indeed, when we plotted the reconstructed geological profiles, the modelled source well reproduced the soil deformation (see the section on DInSAR analyses); therefore, it is likely that the causative fault is mainly represented by the major mechanical discontinuities between some of the Phanerozoic stratigraphic units. The subhorizontal to very low-angle setting and the position of the modelled coseismic slip surface suggest that sliding occurred as a consequence of, and was associated with, a large-scale flexural folding phenomenon affecting the major syncline south of the Handun structure (Figure 13). The general tectonic framework also suggests that beyond the flexural line separating the above-mentioned syncline from the Handun anticline, the flexural sliding also involved

the flank of the latter anticline, progressively evolving to form a cut-through fault crossing its fold core. In this regard, it should be noted that [4] also suggested a similar (though at a minor scale) mechanical behaviour along the shallower southern sector of the Handun anticline (Figure 13b) with the development of a detached back-thrust on the flank of the fold, taking advantage of the locally tilted layering, and, hence, the presence of mechanical discontinuities that are (almost) ideally oriented with the regional compressional stress field. The latter structure proposed in the literature, together with the seismogenic surface proposed in the present paper, forms a sort of distributed shear zone characterised by reverse kinematics and an interland vergence (i.e., back thrusting). Diffuse faulting has also been suggested by [61] based on analogue modelling and field observations.

5. Conclusions

In this study, the doublet earthquakes with magnitudes of M_W 6.0 and 6.4, that struck the Fin area in Hormozgan Province in Iran on 14 November 2021, were analysed. The seismic sequence occurred in a tectonically active area characterised by crustal compression.

The epicentral distribution of the relocated aftershocks (Figure 5) shows that the events spread north of the MFF. The focal mechanism solutions of the doublets were almost identical and in reverse, and both rupture planes showed a similar roughly E–W orientation. In order to better reconstruct the geometry of the causative faults, we investigated the seismicity associated with the seismic sequence by relocating the recorded events, thereby allowing us to constrain their 3D distribution. By plotting the obtained results on some transects crossing the seismogenic volume and running perpendicular to the trace of the MFF (Figure 8), a cluster could be observed suggesting the activation of a S-to-SSW dipping seismogenic shear zone. Among the four cross-sections, numbers 2, 3 and 4 showed a clear view of a previously unidentified south-dipping fault, which is in good agreement with the focal mechanism solutions. Therefore, in contrast with the regional setting of the major faults, the integration of seismicity data next to the focal mechanism solutions confirms the activation of a reverse fault with a southward dip.

The question of the timing of the first basement involvement within the external sectors of the Zagros orogene is still controversial. In this paper, we do not enter this debate, particularly regarding whether these faults have accommodated reverse movements since the beginning of the collision ([67,68]) or whether they were activated only very recently (post-Pliocene) following a Miocene thin-skinned style of deformation, as suggested by [4,11,61]. However, as a major finding of this research, we conclude that both thick- and thin-skinned tectonic styles could be, and indeed are, contemporaneously active within the Zagros Fold-and-Thrust Belt, and this could have a major impact on the seismic hazard assessment of the broader investigated area, especially considering that this composite seismotectonic behaviour likely characterises other sectors of the region.

The activation of the first fault plane could have possibly favoured the occurrence of several aftershocks within the footwall of the Fin doublet system (positive ΔCFF) and triggered the second mainshock (Figure 11). Considering the complex tectonic setting affecting the region, the activation of deep basement faults could favour the dynamic rupture of shallow ones, or vice versa, or at least create the conditions to anticipate forthcoming events.

Author Contributions: Conceptualization and methodology, N.A.F., Z.G. and R.C.; SAR software, N.A.F. and Z.G.; Seismic processing, S.S. and Z.G.; validation, all. All authors contributed to the writing. All authors have read and agreed to the published version of the manuscript.

Funding: This research received no external funding.

Data Availability Statement: Sentinel data were made available by ESA in the Copernicus project through the Open Access Hub portal (https://scihub.copernicus.eu/dhus/#/home (accessed on 25 November 2021)). Seismic data were made available by the IRSC catalogue (www.irsc.ir (accessed on 7 April 2023)) and the IIEES catalogue (www.iiees.ac.ir (accessed on 7 April 2023)) and from one station belonging to the national seismic network of the UAE (https://earthquakes.ncm.ae/ (accessed on 7 April 2023)).

Acknowledgments: Sentinel data, from the ESA Copernicus Project, were obtained through the Open Access Hub. InSAR processing and data modeling were carried out with ENVI® SARscape® (sarmap, CH). Seismic data were obtained from IRSC, IIEES catalogue and national seismic network of UAE.

Conflicts of Interest: The authors declare no conflict of interest.

References

1. IGUT Iranian Seismological Center (Institute of Geophysics, University of Tehran). Available online: http://irsc.ut.ac.ir (accessed on 7 April 2023).
2. IIEES International Institute of Earthquake Engineering and Seismology. Available online: http://www.iiees.ac.ir/fa/recentevents (accessed on 7 April 2023).
3. Hessami, K.; Jamali, F.; Tabasi, H. *Map of Major Active Faults of Iran at 1:2500000*; International Institute of Earthquake Engineering and Seismology (IIEES): Tehran, Iran, 2003.
4. Molinaro, M.; Leturmy, P.; Guezou, J.-C.C.; Frizon de Lamotte, D.; Eshraghi, S.A. The Structure and Kinematics of the Southeastern Zagros Fold-Thrust Belt, Iran: From Thin-Skinned to Thick-Skinned Tectonics. *Tectonics* **2005**, *24*, 1–19. [CrossRef]
5. Jahani, S.; Callot, J.P.; Letouzey, J.; De Lamotte, D.F. The Eastern Termination of the Zagros Fold-and-Thrust Belt, Iran: Structures, Evolution, and Relationships between Salt Plugs, Folding, and Faulting. *Tectonics* **2009**, *28*, 2418. [CrossRef]
6. Berberian, M. Master "Blind" Thrust Faults Hidden under the Zagros Folds: Active Basement Tectonics and Surface Morphotectonics. *Tectonophysics* **1995**, *241*, 193–224. [CrossRef]
7. Molinaro, M.; Zeyen, H.; Laurencin, X. Lithospheric Structure beneath the South-Eastern Zagros Mountains, Iran: Recent Slab Break-Off? *Terra Nova* **2005**, *17*, 1–6. [CrossRef]
8. Jahani, S.; Callot, J.-P.; de Lamotte, D.F.; Letouzey, J.; Leturmy, P. *The Salt Diapirs of the Eastern Fars Province (Zagros, Iran): A Brief Outline of Their Past and Present BT—Thrust Belts and Foreland Basins*; Lacombe, O., Roure, F., Lavé, J., Vergés, J., Eds.; Springer: Berlin/Heidelberg, Germany, 2007; pp. 289–308.
9. Sattarzadeh, Y.; Cosgrove, J.W.; Vita-Finzi, C. The Interplay of Faulting and Folding during the Evolution of the Zagros Deformation Belt. *Geol. Soc. Lond. Spec. Publ.* **1999**, *169*, 187–196. [CrossRef]
10. Molinaro, M.; Guezou, J.C.; Leturmy, P.; Eshraghi, S.A.; de Lamotte, D.F. The Origin of Changes in Structural Style across the Bandar Abbas Syntaxis, SE Zagros (Iran). *Mar. Pet. Geol.* **2004**, *21*, 735–752. [CrossRef]
11. Sherkati, S.; Molinaro, M.; Frizon de Lamotte, D.; Letouzey, J. Detachment Folding in the Central and Eastern Zagros Fold-Belt (Iran): Salt Mobility, Multiple Detachments and Late Basement Control. *J. Struct. Geol.* **2005**, *27*, 1680–1696. [CrossRef]
12. Callot, J.P.; Jahani, S.; Letouzey, J. *The Role of Pre-Existing Diapirs in Fold and Thrust Belt Development BT—Thrust Belts and Foreland Basins*; Lacombe, O., Roure, F., Lavé, J., Vergés, J., Eds.; Springer: Berlin/Heidelberg, Germany, 2007; pp. 309–325.
13. Asghari, A. *Sedimentary Environment, Sequence Stratigraphy and Paleogeography of Paleozoic Pre-Khuff Succession in Southern Iran (Zagros and Persian Gulf)*; Université de Bourgogne: Dijon, France, 2014.
14. Khorrami, F.; Vernant, P.; Masson, F.; Nilfouroushan, F.; Mousavi, Z.; Nankali, H.; Saadat, S.A.; Walpersdorf, A.; Hosseini, S.; Tavakoli, P.; et al. An Up-to-Date Crustal Deformation Map of Iran Using Integrated Campaign-Mode and Permanent GPS Velocities. *Geophys. J. Int.* **2019**, *217*, 832–843. [CrossRef]
15. Agard, P.; Omrani, J.; Jolivet, L.; Whitechurch, H.; Vrielynck, B.; Spakman, W.; Monie, P.; Meyer, B.; Wortel, R. Zagros Orogeny: A Subduction-Dominated Process. *Geol. Mag.* **2011**, *148*, 692–725. [CrossRef]
16. Masson, F.; Anvari, M.; Djamour, Y.; Walpersdorf, A.; Tavakoli, F.; Daignières, M.; Nankali, H.; Van Gorp, S. Large-Scale Velocity Field and Strain Tensor in Iran Inferred from GPS Measurements: New Insight for the Present-Day Deformation Pattern within NE Iran. *Geophys. J. Int.* **2007**, *170*, 436–440. [CrossRef]
17. Masson, F.; Chéry, J.; Hatzfeld, D.; Martinod, J.; Vernant, P.; Tavakoli, F.; Ghafory-Ashtiani, M. Seismic versus Aseismic Deformation in Iran Inferred from Earthquakes and Geodetic Data. *Geophys. J. Int.* **2005**, *160*, 217–226. [CrossRef]
18. Vernant, P.; Chéry, J. Mechanical Modelling of Oblique Convergence in the Zagros, Iran. *Geophys. J. Int.* **2006**, *165*, 991–1002. [CrossRef]
19. Tavakoli-Shirazi, S.; Frizon de Lamotte, D.; Wrobel-Daveau, J.-C.; Ringenbach, J.-C. Pre-Permian Uplift and Diffuse Extensional Deformation in the High Zagros Belt (Iran): Integration in the Geodynamic Evolution of the Arabian Plate. *Arab. J. Geosci.* **2013**, *6*, 2329–2342. [CrossRef]
20. Alavi, M. Structures of the Zagros Fold-Thrust Belt in Iran. *Am. J. Sci.* **2007**, *307*, 1064–1095. [CrossRef]
21. Husseini, M.I. The Arabian Infracambrian Extensional System. *Tectonophysics* **1988**, *148*, 93–103. [CrossRef]
22. Alavi, M. Regional Stratigraphy of the Zagros Fold-Thrust Belt of Iran and Its Proforeland Evolution. *Am. J. Sci.* **2004**, *304*, 1–20. [CrossRef]
23. Blanc, E.; Allen, M.; Inger, S.; Hassani, H. Structural Styles in the Zagros Simple Folded Zone, Iran. *J. Geol. Soc. Lond.* **2003**, *160*, 401. [CrossRef]
24. Berberian, M.; King, G.C.P. Towards a Paleogeography and Tectonic Evolution of Iran. *Can. J. Earth Sci.* **1981**, *18*, 210–265. [CrossRef]

25. Colman-Sadd, S.P. Fold Development in Zagros Simply Folded Belt, Southwest Iran. *Am. Ass. Petrol. Geol. Bull* **1978**, *62*, 984–1003. [CrossRef]
26. Razaghian, G.; Arian, M. The Emergent Salt Diapirs in the East Zagros, Iran. *Open J. Geol.* **2015**, *05*, 718–726. [CrossRef]
27. Fialko, Y.; Sandwell, D.; Simons, M.; Rosen, P. Three-Dimensional Deformation Caused by the Bam, Iran, Earthquake and the Origin of Shallow Slip Deficit. *Nature* **2005**, *435*, 295–299. [CrossRef] [PubMed]
28. Massonnet, D.; Rossi, M.; Carmona, C.; Adragna, F.; Peltzer, G.; Feigl, K.; Rabaute, T. The Displacement Field of the Landers Earthquake Mapped by Radar Interferometry. *Nature* **1993**, *364*, 138–142. [CrossRef]
29. Svigkas, N.; Atzori, S.; Kiratzi, A.; Tolomei, C.; Salvi, S. Isolation of Swarm Sources Using InSAR: The Case of the February 2017 Seismic Swarm in Western Anatolia (Turkey). *Geophys. J. Int.* **2019**, *217*, 1479–1495. [CrossRef]
30. Golshadi, Z.; Rezapour, M.; Atzori, S.; Salvi, S. Multiple Source Analysis from InSAR Data and New Insights into Fault Activation: The 2005 Zarand, Iran, Earthquake. *Terra Nova* **2021**, *33*, 274–283. [CrossRef]
31. Tolomei, C.; Caputo, R.; Polcari, M.; Famiglietti, N.A.; Maggini, M.; Stramondo, S. The Use of Interferometric Synthetic Aperture Radar for Isolating the Contribution of Major Shocks: The Case of the March 2021 Thessaly, Greece, Seismic Sequence. *Geosciences* **2021**, *11*, 191. [CrossRef]
32. Goldstein, R.M.; Werner, C.L. Radar Interferogram Filtering for Geophysical Applications. *Geophys. Res. Lett.* **1998**, *25*, 4035–4038. [CrossRef]
33. Galaktionov, I.; Sheldakova, J.; Toporovskiy, V.; Kudryashov, A. Modified Fizeau Interferometer with the Polynomial and FFT Smoothing Algorithm. In *Interferometry XXI*; SPIE: Bellingham, WA, USA, 2022; Volume 12223, pp. 175–179. [CrossRef]
34. Soncco, D.-C.; Barbanson, C.; Nikolova, M.; Almansa, A.; Ferrec, Y. Fast and Accurate Multiplicative Decomposition for Fringe Removal in Interferometric Images. *IEEE Trans. Comput. Imaging* **2017**, *3*, 187–201. [CrossRef]
35. Ri, S.; Takimoto, T.; Xia, P.; Wang, Q.; Tsuda, H.; Ogihara, S. Accurate Phase Analysis of Interferometric Fringes by the Spatiotemporal Phase-Shifting Method. *J. Opt.* **2020**, *22*, 105703. [CrossRef]
36. Costantini, T.M.; Costantini, M. A Novel Phase Unwrapping Method Based on Network Programming. *IEEE Trans. Geosci. Remote Sens.* **1998**, *36*, 813–821. [CrossRef]
37. Okada, Y. Surface Deformation Due to Shear and Tensile Faults in a Half-Space. *Bull. Seismol. Soc. Am.* **1985**, *75*, 1135–1154. [CrossRef]
38. Atzori, S.; Manunta, M.; Fornaro, G.; Ganas, A.; Salvi, S. Postseismic Displacement of the 1999 Athens Earthquake Retrieved by the Differential Interferometry by Synthetic Aperture Radar Time Series. *J. Geophys. Res. Solid Earth* **2008**, *113*, 5504. [CrossRef]
39. Atzori, S.; Hunstad, I.; Chini, M.; Salvi, S.; Tolomei, C.; Bignami, C.; Stramondo, S.; Trasatti, E.; Antonioli, A.; Boschi, E. Finite Fault Inversion of DInSAR Coseismic Displacement of the 2009 L'Aquila Earthquake (Central Italy). *Geophys. Res. Lett.* **2009**, *36*, 39293. [CrossRef]
40. Foumelis, M.; Parcharidis, I.; Lagios, E.; Voulgaris, N. Evolution of Post-Seismic Ground Deformation of the Athens 1999 Earthquake Observed by SAR Interferometry. *J. Appl. Geophys.* **2009**, *69*, 16–23. [CrossRef]
41. Marquardt, D.W. An Algorithm for Least-Squares Estimation of Nonlinear Parameters. *J. Soc. Ind. Appl. Math.* **1963**, *11*, 431–441. [CrossRef]
42. Chalup, S.; Maire, F. A Study on Hill Climbing Algorithms for Neural Network Training. In Proceedings of the 1999 Congress on Evolutionary Computation-CEC99 (Cat. No. 99TH8406), Washington, DC, USA, 6–9 July 1999; Volume 3, pp. 2014–2021.
43. Li, J.; Li, W.; Huang, R. An Efficient Method for Solving a Matrix Least Squares Problem over a Matrix Inequality Constraint. *Comput. Optim. Appl.* **2016**, *63*, 393–423. [CrossRef]
44. Hernando, L.; Mendiburu, A.; Lozano, J.A. Hill-Climbing Algorithm: Let's Go for a Walk Before Finding the Optimum. In Proceedings of the 2018 IEEE Congress on Evolutionary Computation (CEC), Rio de Janeiro, Brazil, 8–13 July 2018; pp. 1–7.
45. Funning, G.J.; Parsons, B.; Wright, T.J.; Jackson, J.A.; Fielding, E.J. Surface Displacements and Source Parameters of the 2003 Bam (Iran) Earthquake from Envisat Advanced Synthetic Aperture Radar Imagery. *J. Geophys. Res. Solid Earth* **2005**, *110*, 1–23. [CrossRef]
46. Wright, T.J.; Lu, Z.; Wicks, C. Source Model for the Mw 6.7, 23 October 2002, Nenana Mountain Earthquake (Alaska) from InSAR. *Geophys. Res. Lett.* **2003**, *30*, 18014. [CrossRef]
47. Walters, R.J.; Gregory, L.C.; Wedmore, L.N.J.; Craig, T.J.; McCaffrey, K.; Wilkinson, M.; Chen, J.; Li, Z.; Elliott, J.R.; Goodall, H.; et al. Dual Control of Fault Intersections on Stop-Start Rupture in the 2016 Central Italy Seismic Sequence. *Earth Planet Sci. Lett.* **2018**, *500*, 1–14. [CrossRef]
48. Harris, R.A. Introduction to Special Section: Stress Triggers, Stress Shadows, and Implications for Seismic Hazard. *J. Geophys. Res. Solid Earth* **1998**, *103*, 24347–24358. [CrossRef]
49. Hatzfeld, D.; Tatar, M.; Priestley, K.; Ghafory-Ashtiany, M. Seismological Constraints on the Crustal Structure beneath the Zagros Mountain Belt (Iran). *Geophys. J. Int.* **2003**, *155*, 403–410. [CrossRef]
50. Elliott, J.R.; Bergman, E.A.; Copley, A.C.; Ghods, A.R.; Nissen, E.K.; Oveisi, B.; Tatar, M.; Walters, R.J.; Yamini-Fard, F. The 2013 Mw 6.2 Khaki-Shonbe (Iran) Earthquake: Insights into Seismic and Aseismic Shortening of the Zagros Sedimentary Cover. *Earth Space Sci.* **2015**, *2*, 435–471. [CrossRef]
51. Waldhauser, F. *HypoDD-A Program to Compute Double-Difference Hypocenter Locations*; Version 1; Columbia University Libraries: New York, NY, USA, 2001.

52. Waldhauser, F.; Ellsworth, W. A Double-Difference Earthquake Location Algorithm: Method and Application to the Northern Hayward Fault, California. *Bull. Seismol. Soc. Am.* **2000**, *90*, 1353–1368. [CrossRef]
53. Hanssen, R.F. *Radar Interferometry: Data Interpretation and Error Analysis (Remote Sensing and Digital Image Processing)*; Springer: Amsterdam, The Netherlands, 2001; ISBN 9780792369455.
54. Jackson, J.; Fitch, T. Basement Faulting and the Focal Depths of the Larger Earthquakes in the Zagros Mountains (Iran). *Geophys. J. Int.* **1981**, *64*, 561–586. [CrossRef]
55. Baker, C.; Jackson, J.; Priestley, K. Earthquakes on the Kazerun Line in the Zagros Mountains of Iran: Strike-Slip Faulting within a Fold-and-Thrust Belt. *Geophys. J. Int.* **1993**, *115*, 41–61. [CrossRef]
56. Maggi, A.; Jackson, J.A.; Priestley, K.; Baker, C. A Re-assessment of Focal Depth Distributions in Southern Iran, the Tien Shan and Northern India: Do Earthquakes Really Occur in the Continental Mantle? *Geophys. J. Int.* **2000**, *143*, 629–661. [CrossRef]
57. Maggini, M.; Caputo, R. Seismological Data versus Rheological Modelling: Comparisons across the Aegean Region for Improving the Seismic Hazard Assessment. *J. Struct. Geol.* **2021**, *145*, 104312. [CrossRef]
58. Tatar, M.; Hatzfeld, D.; Ghafory-Ashtiany, M. Tectonics of the Central Zagros (Iran) Deduced from Microearthquake Seismicity. *Geophys. J. Int.* **2004**, *156*, 255–266. [CrossRef]
59. Jackson, J.A.; Fitch, T.J.; McKenzie, D.P. Active Thrusting and the Evolution of the Zagros Fold Belt. *Geol Soc Spec Publ* **1981**, *9*, 371–379. [CrossRef]
60. Reasenberg, P.A.; Simpson, R.W. Response of Regional Seismicity to the Static Stress Change Produced by the Loma Prieta Earthquake. *Science* **1992**, *255*, 1687–1690. [CrossRef]
61. Sherkati, S.; Letouzey, J.; de Lamotte, D. Central Zagros Fold-Thrust Belt (Iran): New Insights from Seismic Data, Field Observation, and Sandbox Modeling. *Tectonics* **2006**, *25*, 1766. [CrossRef]
62. McQuarrie, N. Crustal Scale Geometry of the Zagros Fold–Thrust Belt, Iran. *J. Struct. Geol.* **2004**, *26*, 519–535. [CrossRef]
63. Sherkati, S.; Letouzey, J. Variation of Structural Style and Basin Evolution in the Central Zagros (Izeh Zone and Dezful Embayment), Iran. *Mar. Pet. Geol.* **2004**, *21*, 535–554. [CrossRef]
64. Hessami, K.; Koyi, H.A.; Talbot, C.J. The Significance of Strike-Slip Faulting in the Basement of the Zagros Fold and Thrust Belt. *J. Pet. Geol.* **2001**, *24*, 5–28. [CrossRef]
65. Talebian, M.; Jackson, J. A Reappraisal of Earthquake Focal Mechanisms and Active Shortening in the Zagros Mountains of Iran. *Geophys. J. Int.* **2004**, *156*, 506–526. [CrossRef]
66. Leturmy, P.; Molinaro, M.; de Lamotte, D.F. Structure, Timing and Morphological Signature of Hidden Reverse Basement Faults in the Fars Arc of the Zagros (Iran). *Geol. Soc. Lond. Spec. Publ.* **2010**, *330*, 121–138. [CrossRef]
67. Bahroudi, A.; Talbot, C.J. The Configuration of the Basement beneath the Zagros Basin. *J. Pet. Geol.* **2003**, *26*, 257–282. [CrossRef]
68. Mouthereau, F.; Lacombe, O.; Tensi, J.; Bellahsen, N.; Kargar, S.; Amrouch, K. Mechanical Constraints on the Development of the Zagros Folded Belt (Fars). In *Proceedings of the Thrust Belts and Foreland Basins*; Lacombe, O., Roure, F., Lavé, J., Vergés, J., Eds.; Springer: Berlin/Heidelberg, Germany, 2007; pp. 247–266.